# Prediction accuracy of fatigue-relevant load effects in an orthotropic deck

**DOI:**
[10.1016/j.jcsr.2024.108459](10.1016/j.jcsr.2024.108459)

**Document status and date:**
Published: 01/03/2024

**Document Version:**
Publisher's PDF, also known as Version of Record (includes final page, issue and volume numbers)

**Please check the document version of this publication:**

• A submitted manuscript is the version of the article upon submission and before peer-review. There can be important differences between the submitted version and the official published version of record. People interested in the research are advised to contact the author for the final version of the publication, or visit the DOI to the publisher's website.
• The final author version and the galley proof are versions of the publication after peer review.
• The final published version features the final layout of the paper including the volume, issue and page numbers.

[Link to publication](Link to publication)

# Prediction accuracy of fatigue-relevant load effects in an orthotropic deck

Johan Maljaars [a,b,*], Stefan Verdenius [a], Henco Burggraaf [a], Sjors van Es [a]

[a] *TNO, Department Reliable Structures, Molengraaffsingel 8, Delft, 2629 JD, The Netherlands*
[b] *Eindhoven University of Technology, department of the Built Environment, Groene Loper 3, Eindhoven, 5612 AE, The Netherlands*

## ARTICLE INFO

## ABSTRACT

The accuracy of stress estimates in Orthotropic Bridge Decks (OBD) may be negatively impacted by the complex load transfer and asphalt properties. Yet, accurate stress estimates are crucial for optimal fatigue verifications. A field measurement and modelling study has been conducted to evaluate the accuracy of finite element (FE) models. The level of detail of the FE model resembled engineering practice. Measurements comprised of strains caused by normal flowing traffic and by single vehicles with known load. The study gave insight into the distribution of the transverse vehicle location, dynamic vehicle–bridge deck interaction, and the asphalt influence. Comparing with international guidelines, the prediction error of FE models of OBDs is on the edge of acceptable.

## 1. Introduction

It is well known that Orthotropic Bridge Decks (OBDs) are sensitive to fatigue cracking [1,2]. OBDs were traditionally designed for fatigue using approximations of the nominal (i.e., far-field) stress [3]. The Finite Element (FE) method has opened the possibility to design with local or semi-local stress parameters that are deemed to give a more accurate indication of the fatigue-relevant stress ranges. For this reason, more recent studies focus on the fatigue resistance associated with these stress parameters. Examples are fatigue resistances based on the hot-spot stress (HSS) method [4,5], traction stress method [6,7], and the effective notch stress (ENS) method [8,9]. Modern standards and guidelines now also give the possibility to design or assess OBDs with these approaches [10,11].

Application of these approaches in practical designs requires analysis of the (semi–)local stresses in the deck. However, accurate stress prediction is not straightforward because of the complicated three-dimensional load transfer in OBDs, where the load consists of a local load applied on a certain patch – the tyre contact surface – that moves (rolls) over the structure. This creates significant stress gradients in the vicinity of many fatigue-sensitive details [12–14]. The stress is also sensitive to the transverse location of the patch [12,15–22] and the size of the patch [23,24]. Additionally, the asphalt applied on top of most OBDs has a temperature dependent and strain rate dependent stiffness that causes some degree of load distribution in longitudinal and transverse directions [13,23,25–31]. The pavement has a large influence, particularly for weld details in or close to the deck plate, as demonstrated in the above-mentioned studies with asphalt

and with concrete pavement [32–35]. Dynamic interaction between the vehicle and the structure may further affect the stress [16,36]. The resulting complicated stress distribution may cause deviations between the actual stress in an OBD and the engineering prediction thereof using FE models. The uncertainty in strain prediction is the reason that Bridge-Weigh-In-Motion (Bridge-WIM) systems are usually based on measured instead of computed influence lines [20,37–39]. Probabilistic assessments of the fatigue life are also usually based on measured strains [28,29,40,41]. However, measurements are usually not available in the practical fatigue verification of an OBD, which then relies on the accuracy of the FE model.

The ratio between the actual (measured) stress and the engineering estimate thereof is referred to as the model uncertainty (MU). MU comprises the transfer of loads to load effects, including load schematisation. Dynamic interaction is considered here as a separate variable and hence not included in the MU. Studies are conducted to determine the distribution of the MU for the nominal (far-field) stress in bridge components [42] and for the HSS and ENS stress of simple and complex details [43–46]. Results are compared with the MU in guidelines. These guidelines provide a global MU of 0.1–0.2 and an additional MU for the stress concentration factor of 0.05–0.2 [47,48]. Because of the unique structure and load characteristics of OBDs as described above, their MU may deviate from these values. The MU distribution is crucial for estimating reliability and deriving fatigue safety factors [42,49].

The current study aims to evaluate if the MU of FE models of OBDs is within the bounds of the MU set by guidelines [47,48], by comparing predicted strains with measured strains in an OBD. The model contains
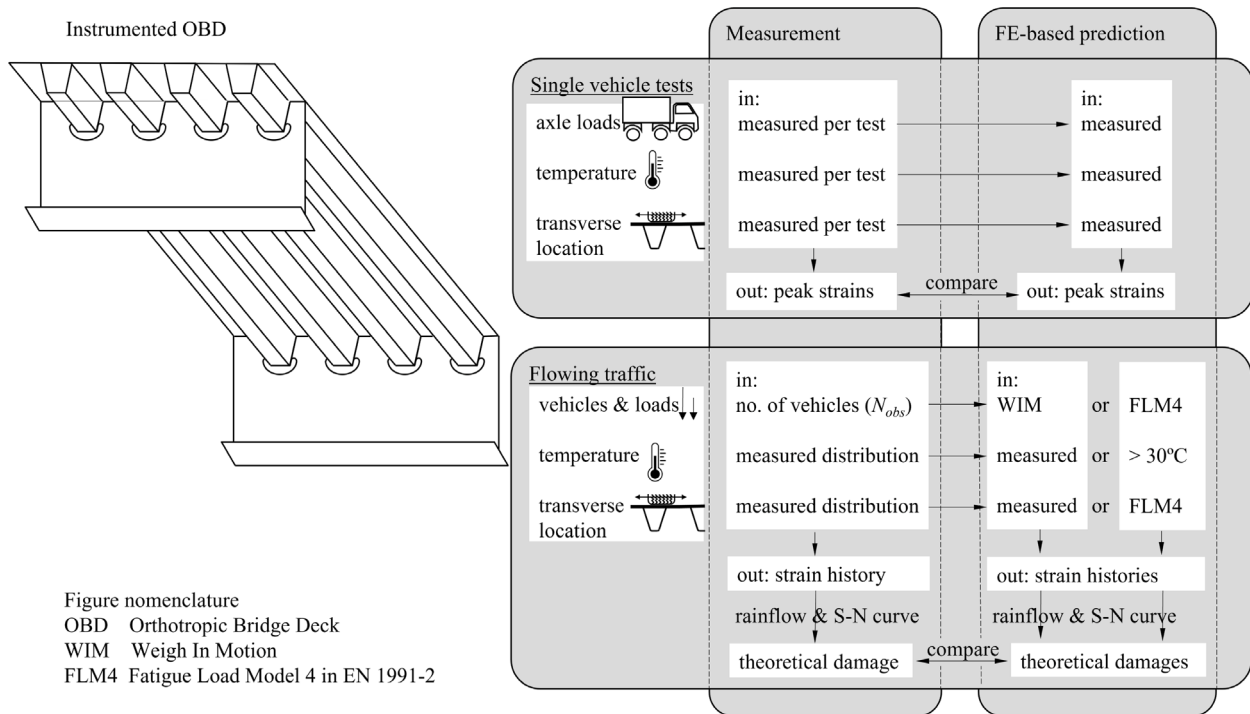
---

**Fig. 1.** Outline of the study. Measured strains resulting from single vehicle tests – with known loads – and flowing traffic are compared with predicted strains and theoretical fatigue damage using an FE model.

assumptions, approximations and levels of detail exemplary for engineering practice. Additional to the MU, the study gives insight into the effects of temperature, dynamic interaction and the transverse location of vehicles on the OBD response.

## 2. Methods and models

### 2.1. Outline

Electric strain gauges and temperature sensors were installed on the OBD of a steel bridge. The gauges measured the strains while a single vehicle with measured tyre loads crossed the bridge. To study the sensitivities listed in Section 1, the vehicle crossed the bridge multiple times with different values for speed, transverse location, and temperature of the deck. Strains were also measured during normal operation of the bridge – with flowing traffic – over a period of one year. A FE model representative of engineering practice was created and used to predict the strains in the OBD caused by the single vehicle and the flowing traffic. Results of measurements and predictions are compared. Effects of dynamics and the model uncertainty are included in a discussion. Fig. 1 summarises the outline of the study.

### 2.2. Lay-out of the instrumented deck

The "Van Brienenoord" bridge crosses the river Maas in Rotterdam, The Netherlands. It consists of two parallel 300 m span arch bridges, one for each traffic direction. Each bridge accommodates two carriageways consisting of three lanes, i.e., twelve lanes in total. The OBD of the considered bridge is constructed from steel grade Fe510 (current equivalent S355) and it consists of a 12 mm thick deck plate supported by trapezoidal ribs with a centre-to-centre distance of 600 mm, see Fig. 2(a) for the rib dimensions. The pavement consists of a mastic asphalt layer with on top a porous asphalt layer with nominal thickness of 30 and 40 mm, respectively. The actual summed thickness of the asphalt layers was measured as 92 mm at the location of study. Sealing sheets are applied between the two asphalt layers and between the
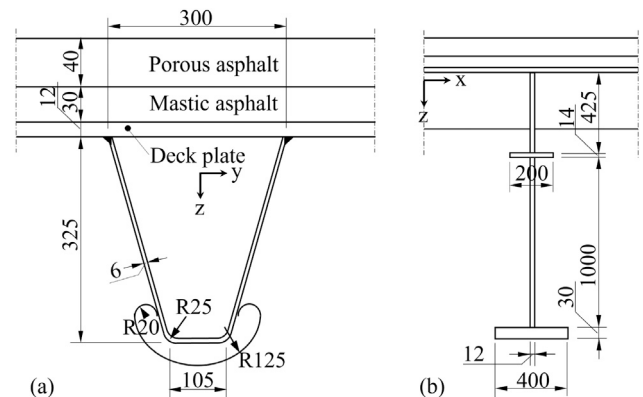


**Fig. 2.** Dimensions [mm] of the deck of the Van Brienenoord bridge: (a) Rib; (b) Crossbeam (subfigures have different scales).

deck plate and the mastic asphalt. Crossbeams transfer the load from the deck to the main girders, see Fig. 2(b) for their dimensions. The measurements were carried out on the part of the OBD below the right lane ("slow" lane, accommodating most of the heavy vehicles) of the long-distance carriageway of the bridge for traffic heading south, relatively close to the expansion joint for entering vehicles. The lane width is 3.3 m.

Fig. 3 shows the positions of the strain gauges. Strain gauges SG1–3 were applied in longitudinal (traffic) direction on the bottom side of the ribs, at midspan between two crossbeams of the first regular deck span (approximately 4.5 m from the expansion joint) and SG34/35/37 were applied at midspan between two crossbeams further away (approximately 28 m) from the expansion joint. The two groups were applied to evaluate if the expansion joint causes an additional dynamic effect. Each group consisted of three adjacent instrumented ribs with the centre one closest to the centre of the right tyres of most heavy vehicles, see Fig. 3. The three gauges allowed to evaluate the relative
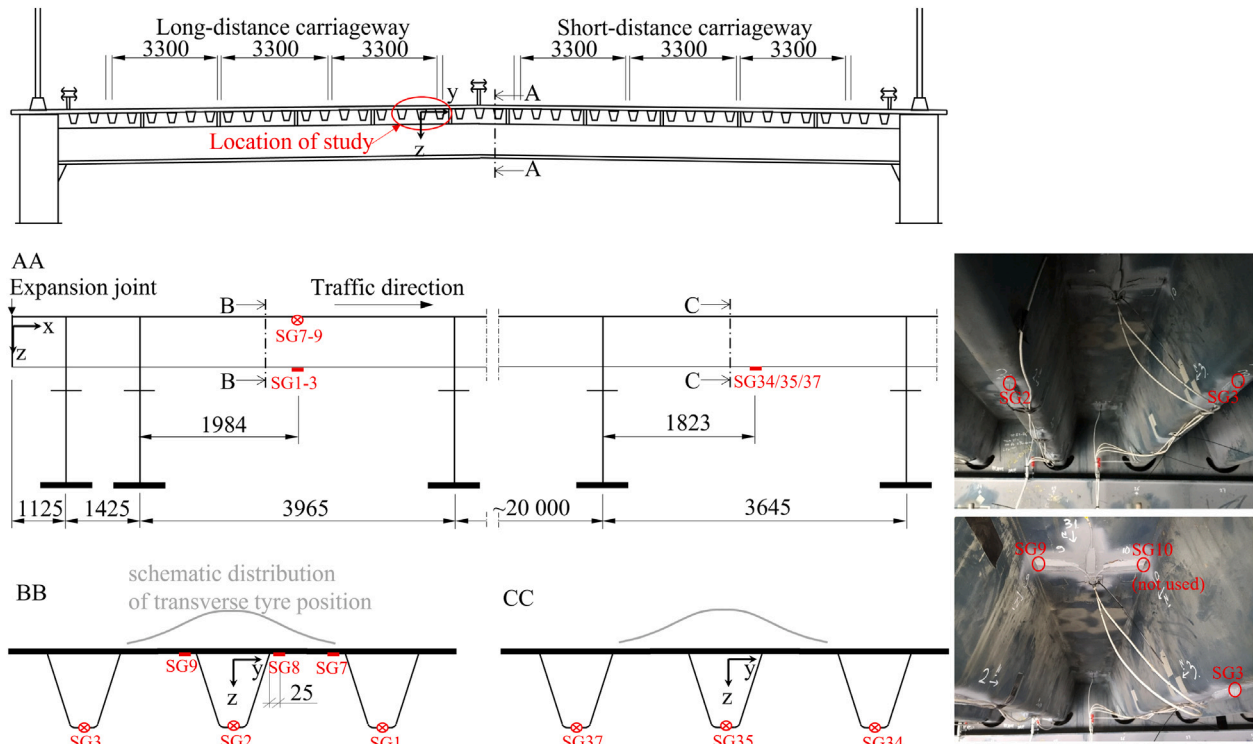
**Fig. 3.** Locations of the applied strain gauges (SG) (dimensions [mm]).

share of the load between the three ribs as a function of the transverse location of the tyre. Strain gauges SG7–9 were applied in transverse direction to the bottom of the deck, also at midspan between two crossbeams, and approximately 25 mm from the toe of the weld with the rib. They have a shorter influence field and they are more sensitive to the tyre patch, transverse location and asphalt stiffness than SG1–3/34/35/37. Strains were recorded with a frequency of 600 Hz and a low-pass filter of 50 Hz was applied.

### 2.3. Description of the engineering FE model

A FE model consisting of the OBD including crossbeams and asphalt was created using the software DIANA 9.4.4 [50]. The model was aimed at reflecting engineering practice, not at creating the most accurate representation of reality. It was inspired on FE models that the authors have seen in practice for designs and assessments of OBDs.

Most studies use a detailed model for the deck, whereas the main load bearing structure is modelled with various levels of detail, or not modelled at all [37,51], depending on the strain levels caused by vehicles further away from the point of interest [37,52]. The main load bearing structure was not modelled in the current study, because a preliminary study showed the strains in the OBD resulting from global deflection to be negligibly small. The crossbeams were modelled as constrained against rotation about their strong axis and against vertical translation at their ends (i.e., restrained for rotation around the bridge axis) to reflect the high torsional stiffness of the main girders. The model aimed at predicting the strains at the distance of 4.5 m from the expansion joint, see Fig. 4. Horizontal translation of the deck in the bridge span direction was constrained at the model end opposite to the expansion joint.

A relatively coarse mesh (see Fig. 4) consisting of thin quadrilateral shell elements with quadratic shape function and 2x2 integration – type CQ40S – was used for the steel structure. The steel Youngs modulus was assumed as 210 GPa and the Poisson ratio was 0.3. The two asphalt layers were modelled separately, each consisting of one layer

**Table 1**
Asphalt Youngs modulus [GPa] used in the model.

| Asphalt | Temperatures | | |
|---|---|---|---|
| | 0 °C | 15 °C | 30°C |
| Mastic (bottom – 30 mm) | 17.0 | 8.1 | 0.1 |
| Porous (top – 40 mm) | 8.8 | 4.3 | 0.1 |

of hexahedron solid elements with quadratic shape function and 3x3x3 integration – type CHX60. Their thickness was the nominal thickness (70 mm). The Youngs modulus of asphalt mixtures used on OBDs depends on the temperature, strain rate, and mixture composition [26,30,53]. In agreement with engineering practice in The Netherlands, the Youngs modulus was temperature dependent with values from tests on typical asphalt mixtures applied in The Netherlands [54], but negligibly low at $\geq 30°C$, see Table 1. The asphalt strain rate sensitivity was not modelled, but modulus values were taken at strain rates representative of a vehicle speed of 80 km/h because most vehicles travel close to this speed limit. The asphalt Poisson ratio was taken as 0.35, reflecting an average value at relevant strain rates in [55,56]. Sealing sheets were modelled with interface elements of type CQ48I. Their traction stiffness in normal direction was taken as 100 times the asphalt Youngs modulus divided by their thickness of 1 mm (preventing flexibility) and it was negligibly small in shear direction, mimicking non-composite action between steel and asphalt. Dynamic interaction between vehicle and structure was not modelled.

Influence lines were computed with the model for the three different temperatures of Table 1, for seven transverse locations (with the right tyres central above the rib of SG2, and 150, 300 and 450 mm to either side of that rib), and for two tyre patches, namely, double patches of 300 mm x 250 mm with 100 mm in between for the double tyre axles and single patches of 300 mm x 330 mm for single tyre axles, see Fig. 5(a). Following EN 1991-2 [57], the centres of the patches are aligned in transverse direction (patch areas deviate from [57].)
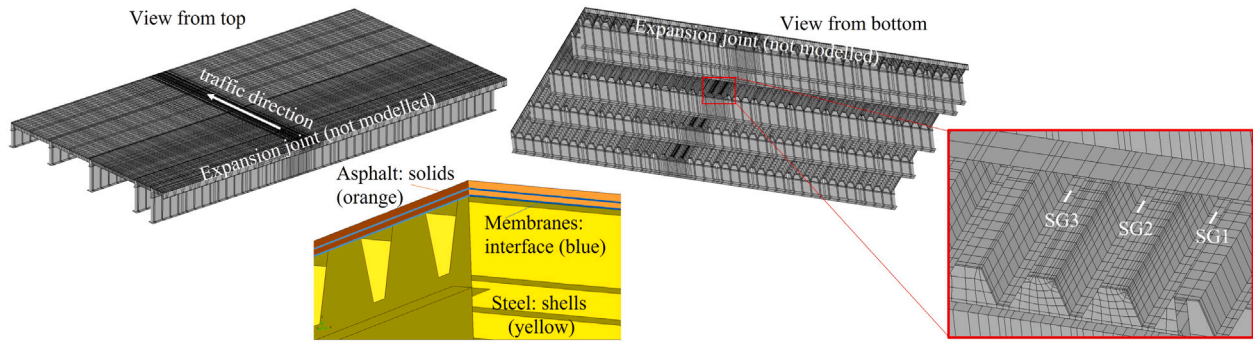
**Fig. 4.** Lay-out of the FE model, representative for engineering practice: relatively coarse mesh with thin quadratic shell elements for steel structure, solid elements for asphalt layers and interface elements for sealing sheets.
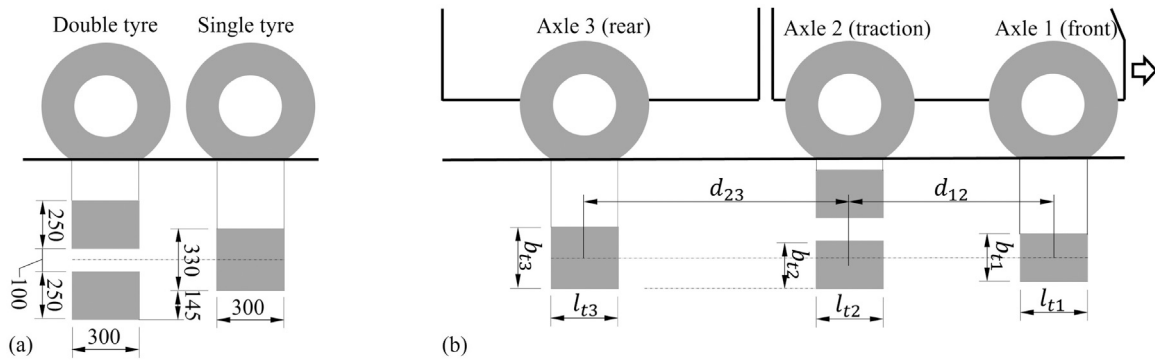


**Fig. 5.** Tyre patches (not drawn on scale): (a) Used in the model, dimensions in mm; (b) Of the test vehicle, dimensions in Table 3. Differences in axle alignment and small differences in patch areas exist between the test vehicle and the model.

**Table 2**
Measured temperatures during the single vehicle tests.

| Test series | Date | $T_{deck}$ [°C] | $T_{asphalt}$ [°C] |
|---|---|---|---|
| Summer day | 2018–07–26 | 25–34 ($\mu = 30$; $\sigma = 3.2$) | 34–47 ($\mu = 40$; $\sigma = 4.5$) |
| Summer night | 2018–08–31 | 12–14 | 11–13 |
| Winter night | 2019–02–16 | 5–7 | 5–6 |

**Table 3**
Vehicle characteristics of the single vehicle tests.

| Test series | $F_{t1}$ [kN] | $2F_{t2}$[a] [kN] | $F_{t3}$ [kN] | $l_{t1}$ [mm] | $l_{t2}$ [mm] | $l_{t3}$ [mm] | $b_{t1}$ [mm] | $2b_{t2}$ [mm] | $b_{t3}$ [mm] | $d_{12}$ [m] | $d_{23}$ [m] |
|---|---|---|---|---|---|---|---|---|---|---|---|
| Summer day | 33.5 | 38.0 | 55.2 | 260 | 210 | 305 | 260 | 2 × 270 | 325 | 3.80 | 4.78 |
| Summer night | 31.2 | 48.6 | 51.2 | 250 | 210 | 275 | 250 | 2 × 250 | 300 | 3.80 | 6.25 |
| Winter night | 32.4 | 36.3 | 66.7 | 255 | 200 | 300 | 275 | 2 × 275 | 335 | 3.78 | 4.77 |

[a] Listed is the summed load of the two tyres of the right side of the double-tyre axle.

### 2.4. Single vehicle tests

Measurements were performed during the crossing of a vehicle with measured axle loads at three dates. The air temperatures during the three dates were different, so that data were obtained at different stiffness values of the asphalt. The dates are referred to as 'summer day', 'summer night' and 'winter night'. Table 2 gives the temperature of the top side of the asphalt, $T_{asphalt}$ and the bottom side of the deck plate, $T_{deck}$, measured with temperature sensors. The table provides temperature ranges and, for the summer day tests, the average ($\mu$) and standard deviation ($\sigma$) because the measurements required several hours during which the temperature fluctuated significantly. The three-axle air-suspended vehicles used in the tests differed between the summer day/night and the winter night tests, with tyre loads $F_t$, tyre patch length $l_t$, tyre patch width $b_t$ and axle distances $d$ given in Table 3, see Fig. 5 for symbols definition. These patches deviate from those applied in the FE model because the model was made prior to the measurements, thereby preventing undesired prior knowledge in generating the model. The patch area of the third axle – which will be mainly used in the comparisons in the next section – in the model was 1.00, 1.21 and 0.98 times the patch area of the summer day tests, the summer night tests and the winter night tests, respectively.

The vehicles crossed the bridge at speeds of $v \approx 80$ km/h at all dates and additionally at $v \approx 20$ km/h during the nocturnal measurements (not possible during the day due to bridge operational constraints). Two additional measurements were carried out with a still standing vehicle ($v = 0$ km/h) during the winter night. Each crossing was repeated several times with different transverse location of the vehicle. The location was measured using an action camera, a GPS-based system and a laser during the summer day, summer night and winter night tests respectively, where the latter systems were deemed more accurate. The test programme hence covers the relevant parameters speed, temperature and transverse tyre location.

### 2.5. Flowing traffic measurements

Strains and temperatures were measured during one year of bridge operation. Peak and trough values were determined from the strain history and processed with a rainflow counting algorithm to obtain strain spectra. The number of heavy vehicles, $N_{Obs}$, was taken as the number of vehicles with at least one tyre load exceeding a threshold value. The transverse location of that same tyre was estimated by the ratio of strains between SG1–3, using an algorithm described in Appendix.

Strains were also predicted with the FE model of Section 2.3 for the vehicles of a Weigh In Motion (WIM) database described in [58]. The WIM station is located approximately 40 km away from the bridge, with several highway junctions in between. The distributions of load
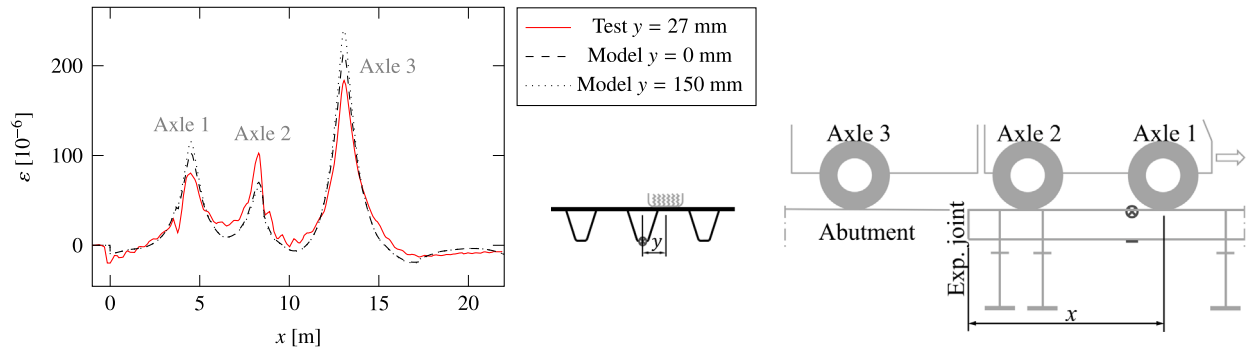
**Fig. 6.** Measured and predicted strains, $\epsilon$, of SG2 of one of the summer day tests ($v = 80$ km/h). The three axles are clearly visible. The model overestimates the strains for the first and third axle but underestimates the strains for the second axle.

**Table 4**
Number of axles $n_{ax}$, axle loads $F_{ax}$, axle distances $d_{ax}$, and fraction of vehicles for long distance traffic $f$, of the five vehicles comprising FLM4.

| $n_{ax}$ [−] | $F_{ax}$ [kN] | Axle type[a] | $d_{ax}$ [m] | $f$ [−] |
|---|---|---|---|---|
| 2 | 70; 130 | S; D | 4.5 | 0.20 |
| 3 | 70; 120; 120 | S; D; D | 4.2; 1.3 | 0.05 |
| 5 | 70; 150; 90; 90; 90 | S; D; S; S; S | 3.2; 5.2; 1.3; 1.3 | 0.50 |
| 4 | 70; 140; 90; 90 | S; D; D; D | 3.4; 6.0; 1.8 | 0.15 |
| 5 | 70; 130; 90; 80; 80 | S; D; S; S; S | 4.8; 3.6; 4.4; 1.3 | 0.10 |

[a] S = single tyres (two tyres per axle); D = double tyres (four tyres per axle).

and vehicle composition are deemed representative but the number of heavy vehicles may deviate between the bridge and the WIM database. The number of heavy vehicles of the WIM database was therefore scaled to match $N_{Obs}$. An algorithm previously developed and validated against strain measurements on a bridge [58] was used to run the array of axles of the WIM database over the influence field computed with the FE model. Each of the vehicles was assigned a transverse location and an asphalt temperature according to either literature-based or measured distributions. Because a limited number of influence lines was computed, linear interpolation was applied for the transverse location and quadratic interpolation was applied for the temperature (exponential interpolation was also considered and it gave almost identical results). Rainflow counting was applied to derive the strain range histogram from the resulting strain history. Additional to the WIM database, strains were simulated for Fatigue Load Model 4 (FLM4) of the European standard EN 1991-2 [57]. FLM4 consists of five vehicles of different configuration, axle load, and quantity, see Table 4. This load model has been developed for details with short influence lines, relevant for OBDs.

The measured strain ranges were transferred to stress ranges by multiplying them with the Youngs modulus of 210 GPa. This is deemed appropriate because the stress state is (close to) uniaxial for all strain gauge locations. The measurement and the prediction of the full year flowing traffic were compared in terms of theoretical fatigue damage $D$. This damage was determined using the linear damage accumulation rule of Palmgren and Miner [59,60] and an assumed bi-linear S–N curve with slope parameters typical for welded details:

$$D = \sum_{i=1}^{n} 1/N_i \tag{1}$$

$$\log_{10}(N_i) = \begin{cases} 12.30 - 3\log_{10}(\Delta s_i/\text{MPa}) & \text{if } \Delta s_i \geq 74\text{MPa} \\ 16.04 - 5\log_{10}(\Delta s_i/\text{MPa}) & \text{if } \Delta s_i < 74\text{MPa} \end{cases} \tag{2}$$

where $n$ is the total number of cycles and $N_i$ is the number of cycles to failure of a cycle $i$ with stress range $\Delta s_i$. This S–N curve describes FAT class 100 with a knee-point at $5 \cdot 10^6$ cycles. The actual FAT class of

OBD details generally differs from the value considered [11], but the influence is limited (provided the actual FAT class does not deviate too much) because the results are presented in terms of ratio of damage between computed and measured strains.

## 3. Results of single vehicle tests

### 3.1. Measurements

As an exemplary result, the red curve in Fig. 6 presents the recorded strain $\epsilon$ of SG2 during one of the summer day tests, where $x$ is the distance between the front axle and the expansion joint. The transverse location of the centre of the right tyre of the rear axle was measured as $y = 27$ mm from the centre of the rib. The peaks caused by the three axles are clearly distinguishable.

The maximum strain recorded for the rear axle of each test (for the three dates, the two vehicle speeds and all transverse locations) is considered hereafter. The dots in Fig. 7 present the ratio between this strain for SG1–3 and the tyre load as a function of the measured transverse location. The following observations are made:

- The share of each rib in transferring the load depends on the transverse location.
- The temperature also influences the distribution of load between the ribs. Higher maximum strains are measured at high temperature compared to low temperature for the decisive transverse location. This demonstrates the influence of the temperature-dependent asphalt stiffness: the load is more equally distributed between the three ribs at low temperature (high asphalt stiffness), whereas a single rib transfers a major fraction of the load at high temperature.
- A moderate difference in strain results between the crossings at low speed and at high speed. The crossings at $v = 80$ km/h give a slightly *lower* strain than at 20 km/h for the same temperature and transverse location. This observation applies close to the expansion joint (Fig. 7) and further away from it (Fig. 8). A similar observation of lower strains measured at higher vehicle speed was made in [61–63], which is at least partially caused by the strain rate sensitivity of the asphalt stiffness. This is further confirmed with the still-standing vehicle, which gives a higher maximum strain compared to the crossings at $v = 20$ km/h and 80 km/h at the same temperature (green filled symbols).

The red curves in Fig. 9 present the recorded strains of SG9 – deck plate in transverse direction – of four summer day tests with different transverse locations. Because of their local nature, the strains significantly depend on the transverse location; stress peaks may even change sign. Figs. 10 and 11 give the minimum and maximum strains
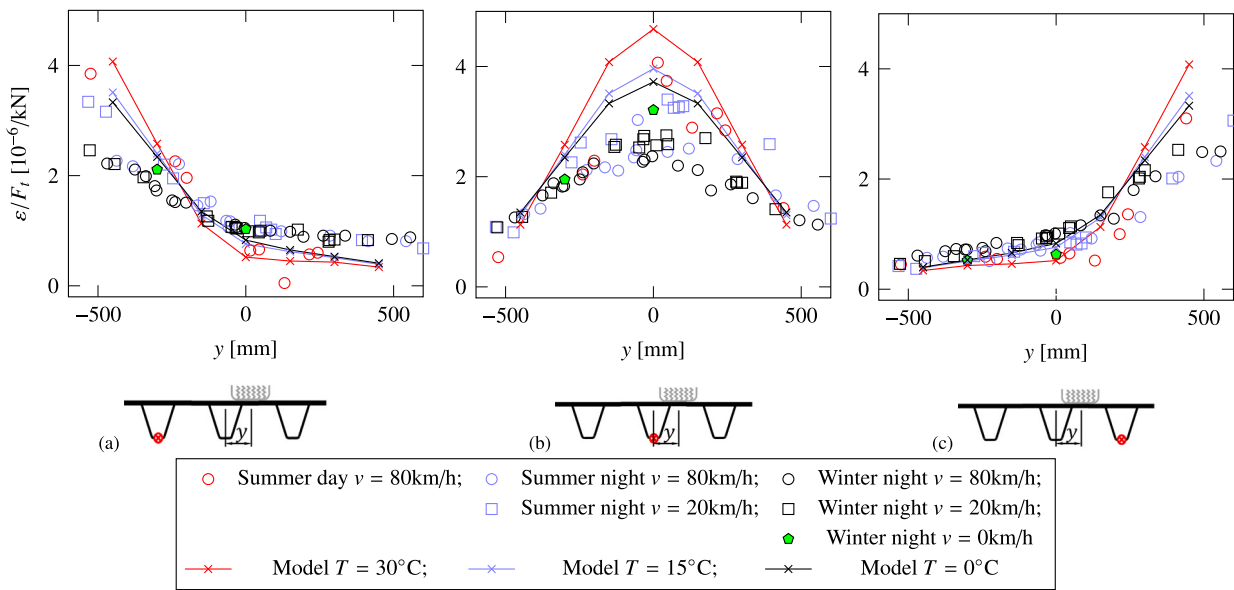
**Fig. 7.** Maximum strain divided by tyre load for SG1–3 according to the tests (dots) and the model (curves): (a) SG3; (b) SG2; (c) SG1. A clear influence of the tyre transverse location $y$, temperature $T$, and vehicle speed $v$ is observed. The model predicts higher maximum strains for the decisive transverse location, possibly due to an underestimation of the asphalt or sealing sheet shear stiffness.
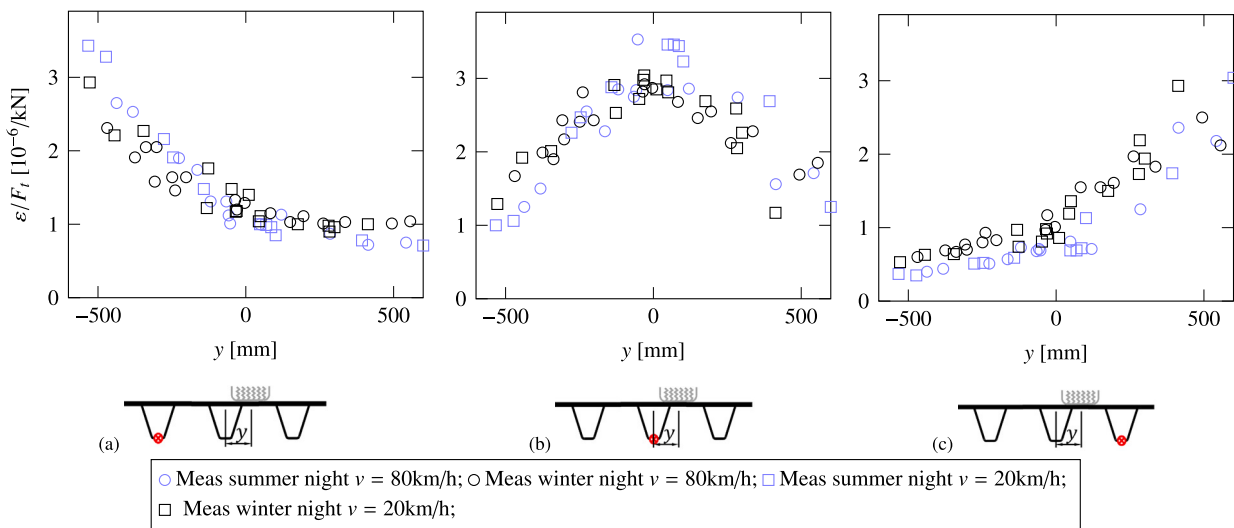


**Fig. 8.** Maximum strain divided by tyre load for SG34/35/37 according to the tests: (a) SG37; (b) SG35; (c) SG34. The trends are the same as for SG1–3 (Fig. 7). The strains at high vehicle speed are slightly *lower* compared to low speed.

of SG7–9 of all tests. The large influence of temperature is caused by the increased flexibility of the deck at increased temperature. The same quantitative trends are observed as for SG1–3, but the influence of temperature (i.e., asphalt stiffness) is larger for SG7–9.

### 3.2. Model prediction

The two black curves in Fig. 6 present the predicted strains for the two closest computed transverse locations using the model. The predicted strains are in qualitative good agreement with the tests, but there are quantitative differences. The model predicts a higher strain compared to the test for the single tyre front and rear axles, but a lower strain for the double tyre traction axle. The underestimation of strain of the double tyre axle is caused by transverse alignment of the centres of single and double tyre axles in FLM4, Fig. 5(a), causing a much larger width for double tyre axles compared to single tyre axles. The axle width difference is smaller for the test vehicle, Fig. 5(b), and

for most vehicles, [24]. Consequently, one of the tyres is running over the rib of SG2 in the test whereas the two tyres are located either side of that rib in the model.

The curves in Fig. 7 present the predicted peak strains of the rear axle. The maximum predicted peak strains over all transverse locations are higher and the load is less equally distributed between the ribs compared to the tests. Likely explanations are a too low asphalt stiffness or sealing sheet shear stiffness in the model. A sensitivity study to these aspects is given below.

Model results are also added to Figs. 9–11. The predicted strains are in qualitative good agreement with the tests. Both tests and model predict a non-linear trend between minimum strain and temperature, where the minimum strains during the winter night and summer night tests are marginal compared to the strains during the summer day tests. However, the quantitative differences between measurements and model are larger for SG9 (deck plate) than for SG2 (rib bottom).

The smaller predicted influence of asphalt stiffness compared to the test may be due to uncertainty in the asphalt Youngs modulus, the
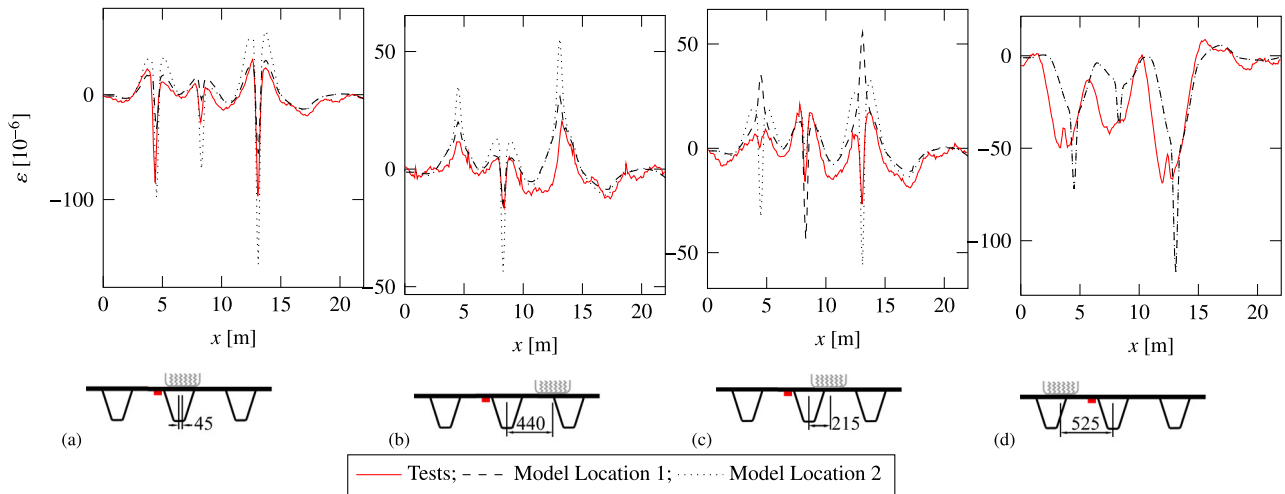
**Fig. 9.** Measured and predicted strains $\varepsilon$ of SG9 of four summer day tests with different transverse locations ($v = 80$ km/h): (a) $y = 45$ mm (model 0 and 150 mm); (b) $y = 440$ mm (model 300 and 450 mm); (c) $y = 215$ mm (model 150 and 300 mm); (d) $y = -525$ mm (model -500 mm). The results are in qualitative good agreement. The strains are sensitive to the transverse location.
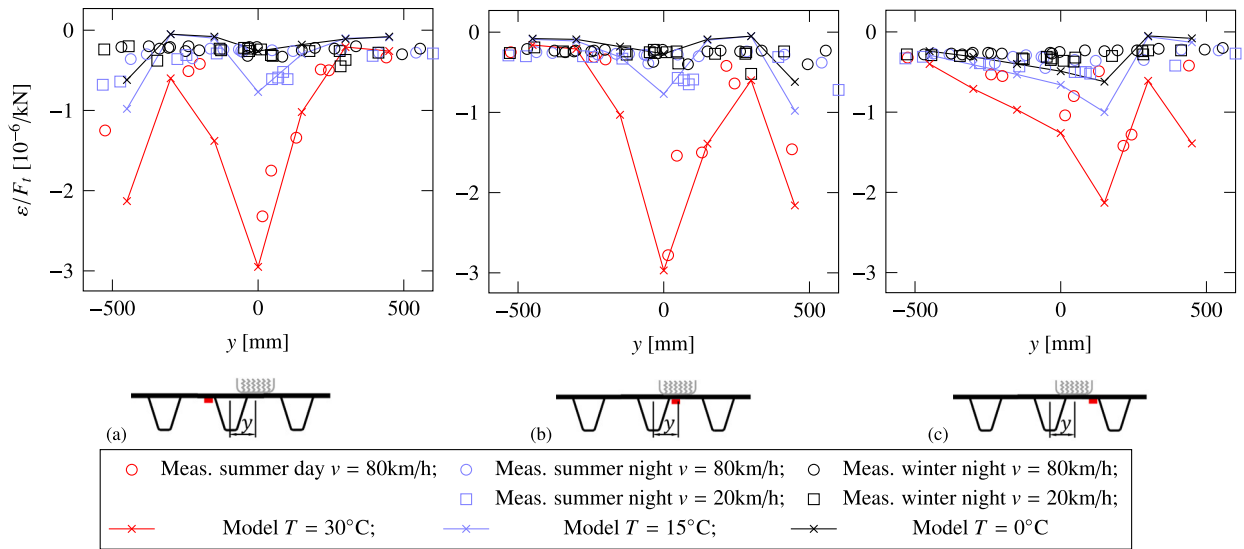


**Fig. 10.** Minimum strain divided by tyre load for SG7–9 according to the tests (dots) and the model (curves): (a) SG9; (c) SG8; (d) SG7. The minimum strains at high temperature are much higher than at other temperatures.

difference between the nominal and the measured asphalt thickness ($h_a = 70$ mm and 92 mm, respectively) and/or the shear stiffness of the sealing sheets, which influences the composite action [31]. Variants of the FE model were made to evaluate the sensitivity to these properties:

- The nominal asphalt thickness (70 mm) was replaced with the measured thickness (92 mm), assuming that the ratio of thickness of the two asphalt layers is as for the nominal case.
- The nil shear stiffness of the sealing sheets was replaced with a shear stiffness equal to that of the asphalt (real stiffness expected in between the two variants [26]).

The results of the predictions with these variants showed that the strains are insensitive to the asphalt thickness and sealing sheet stiffness at a temperature of 30°C, when the asphalt stiffness is negligible: the maximum variation in strain was less than 1% and 8% for SG2 and SG9, respectively. Additional local FE models were constructed with more elements over the asphalt thickness, confirming the insensitivity. A larger influence on strain was found at lower temperatures, especially for SG9, but the effect on total fatigue damage of strain ranges at low temperatures is marginal, as will be demonstrated in the next section.

## 4. Results of the traffic flow measurements

### 4.1. Distributions of temperature and transverse location

The previous section demonstrated that the strain depends on temperature and transverse location of the tyre. Simulating traffic flow therefore requires the distributions of these variables for the entire traffic volume. These distributions are estimated from the strain gauge measurements with the algorithm in Appendix.

The annual number of vehicles on the slow lane estimated with that algorithm and with at least one single-tyre axle load $F_{ax}$ exceeding 45 kN or 60 kN was 0.94 million or 0.45 million, respectively. The former number is used as an estimate of the annual number of heavy vehicles $N_{Obs}$. Predictions with the influence lines of the two measured locations and the WIM database demonstrate that the latter group causes between 90% and 95% of the total theoretical fatigue damage. Fig. 12(a) provides the Probability Density Function (PDF) of the estimated (strain gauge (Appendix) based) vehicles with $F_{ax} > 60$ kN as a function of the temperature at which they were recorded. The distribution using the temperature at the top of the asphalt (solid curve)
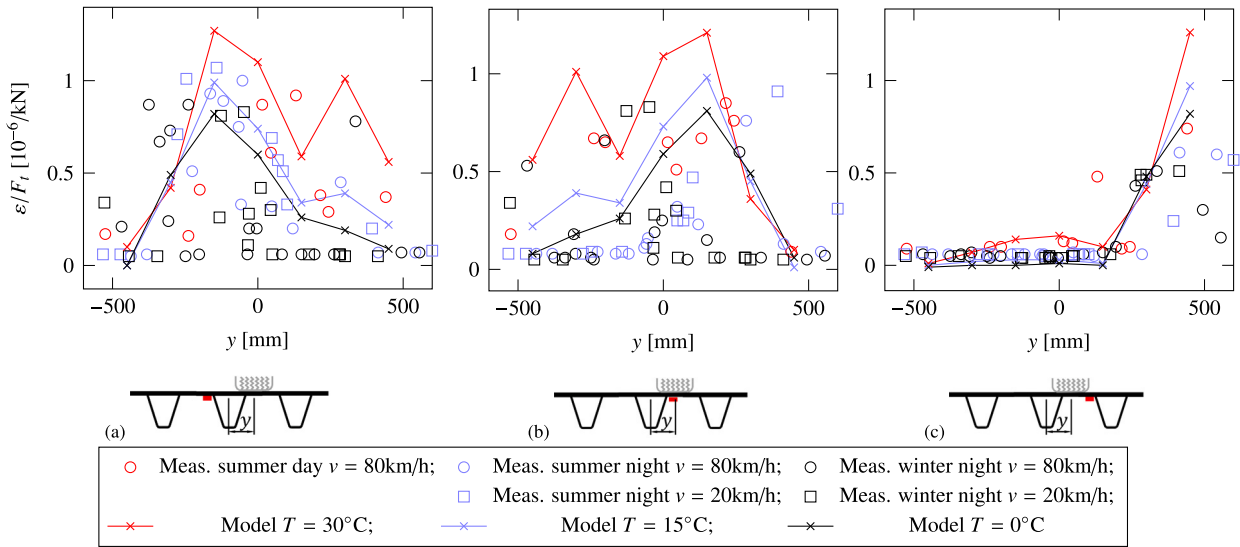
**Fig. 11.** Maximum strain divided by tyre load for SG7–9 according to the tests (dots) and the model (curves): (a) SG9; (b) SG8; (c) SG7. The effect of temperature is less pronounced as compared to the minimum strain (Fig. 10).
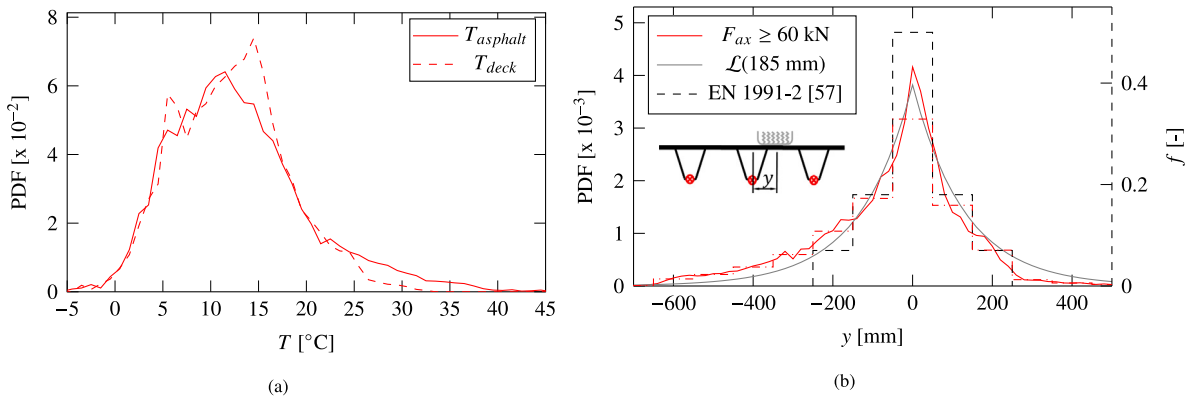


**Fig. 12.** Probability Density Functions (PDF) of vehicles with $F_{ax} > 60$ kN estimated from the flowing traffic measurements: (a) As function of temperature, showing a larger high-temperature tail for the asphalt compared to the steel deck; (b) As a function of the transverse location, with EN 1991-2 [57] giving a narrower distribution.

is comparable to that using the deck plate temperature (dashed curve), but it has a larger tail with high temperatures. This is attributed to solar radiation; a similar influence as obtained here is reported in [28]. The solid curve in Fig. 12(b) provides the PDF of vehicles with $F_{ax} > 60$ kN as a function of the estimated (strain gauge based) transverse tyre location. This distribution has a standard deviation $\sigma = 185$ mm and a skewness of 0.5. Ignoring the skewness, a Laplace distribution gives a reasonable fit of the data (denoted with $\mathcal{L}(185$ mm)). The dashed black curve in the same figure gives the frequency of transverse location in 100 mm bins according to EN 1991-2 [57] (right ordinate). This distribution is significantly narrower – $\sigma = 100$ mm – than the measurement (dashed red curve, representing the measurement in bins).

### 4.2. Measured stress range spectra

Fig. 13(a) presents the stress range spectra of the year-around flowing traffic measurement of SG2. The spectra are grouped in bins of asphalt temperature. Fig. 13(b) gives the same data but normalised: the cumulative number of cycles is divided by the recorded number of

vehicles at the same temperature range. As expected, higher temperatures cause larger stress ranges. This is more pronounced for the deck plate strain gauge SG9, see Fig. 13(c) (same temperature sensor).

### 4.3. Damage based on measurement and FE prediction

The theoretical fatigue damage is predicted to evaluate the impact on fatigue, with the procedure explained in Section 2.5. Fig. 14 gives the resulting damage values for SG2 and SG9. Whereas the damage varies approximately linearly with temperature for SG2, the damage for SG9 is dominated by the high temperatures. The damage contribution of a vehicle at 50°C is 4 orders of magnitude higher than that of the same vehicle at −10°C for SG9 and 1.5 order of magnitude – still significant – for SG2.

The theoretical damage was also determined using the influence fields determined by the FE model, as explained in Section 2.5. Table 5 presents the ratio between the theoretical damage predicted with the model – using different assumptions – and the theoretical damage using the measured stress spectra. The cases are ordered from the simplest
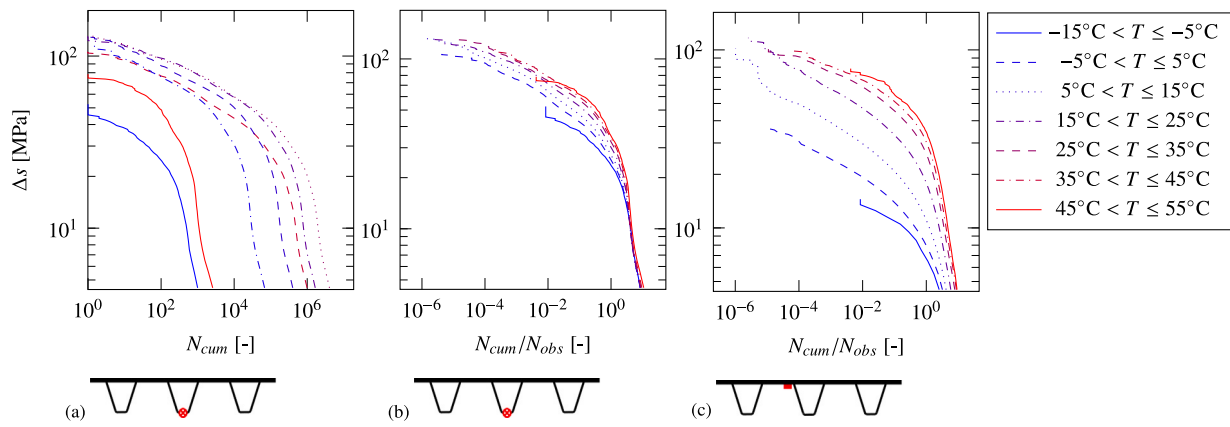
**Fig. 13.** Stress range spectrum: (a) stress ranges $\Delta s$ versus cumulative number of cycles $N_{cum}$ for SG2; (b) $\Delta s$ versus cumulative number of cycles divided by the number of heavy vehicles $N_{cum}/N_{obs}$ for SG2; (c) $\Delta s$ versus $N_{cum}/N_{obs}$ for SG9. A vehicle causes higher stress ranges at high temperatures than at low temperatures.
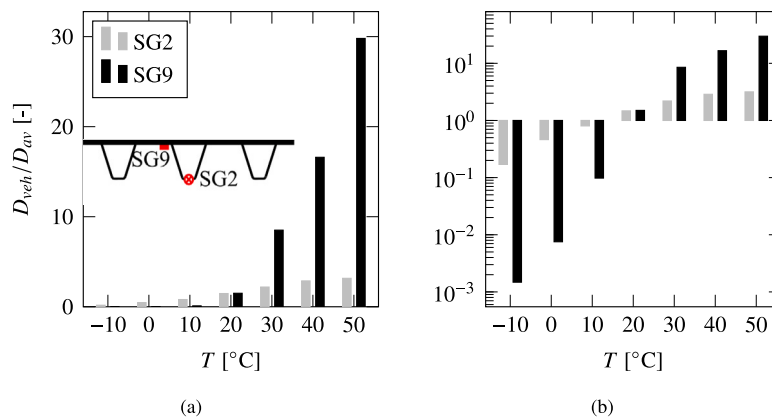


**Fig. 14.** Theoretical, average damage per heavy vehicle and per temperature bin relative to average damage per heavy vehicle: (a) linear scale; (b) semi log scale. The damage at 50°C is orders of magnitude larger than that at −10°C for SG9.

**Table 5**
Ratio between predicted damage using the FE model $D_{FE}$ and the theoretical damage using measured strains of the flowing traffic $D_{meas}$.

| Load model[a] | Temperature | Transverse location | $D_{FE}/D_{meas}$ | |
|---|---|---|---|---|
| | | | SG2 | SG9 |
| FLM4 | ≥ 30°C | Most adverse | 16 | 74 |
| FLM4 | ≥ 30°C | EN 1991-2 [57] | 9.3 | 51 |
| FLM4 | ≥ 30°C | Measured (Fig. 12(b)) | 8.8 | 42 |
| FLM4 | Measured (Fig. 12(a)) | Measured (Fig. 12(b)) | 5.5 | 2.9 |
| WIM data | Measured (Fig. 12(a)) | Measured (Fig. 12(b)) | 1.3 | 0.7 |

[a] Number of vehicles scaled to match the measurement: 0.94 million annually.

engineering approximation to closest to reality. The table shows that the damage ratios reduce accordingly, with the latter values closest to unity. The table further demonstrates the large influence on the fatigue damage of all three parameters. Note that FLM4 contains a level of conservatism, required to meet the reliability level set in the Eurocodes [42].

## 5. Discussion

### 5.1. Estimates of temperature and transverse location

Table 5 demonstrates the importance of the temperature and the transverse location. Measurements of temperature and transverse location are usually not available for practical designs or assessments. One then must rely on data from standards or literature.

As a simplification of the temperature-dependent asphalt influence, some authors do not explicitly model asphalt but assume a dispersion of tyre patches through the asphalt layer with a slope of 1 to 1 [21,22]. The model in the current study demonstrates that this is too optimistic at high temperatures. Detailed FE models of asphalt on OBDs [64,65] confirm this finding. An accurate fatigue damage prediction therefore requires a prediction of the number of vehicles as a function of temperature. Several authors have provided estimates of the steel temperature distribution, but the application is usually limited to one bridge (or regional climate). As an exception, [64,66] propose a model for the distribution of heavy vehicles over temperature, based on the annually and daily fluctuating air temperature and radiation. The black solid curve in Fig. 15(a) provides the PDF resulting from this model. Compared to the measurements (red curves), the model prediction appears not accurate; it overestimates the fraction of vehicles at high temperatures. The grey dashed and dotted curves give the air temperature $T_{air}$ during the year of study and the average of the years 2010–2020, respectively, as measured by the Dutch meteorological institute in the bridge region [67]. The two grey curves are in close agreement, indicating that the year of study has mean air temperatures. These curves are close to the dashed red curve, i.e., the number of vehicles per temperature of the deck plate can be estimated from the air temperature distribution. However, radiation increases the upper tail of the asphalt temperature distribution and it should be accounted for to prevent non-conservative verifications. Differences between bridges may be present due to variations in the temperature-dependent asphalt properties, the composite action related to the sealing sheet stiffness, the actual versus the nominal asphalt thickness, but also due to its age,
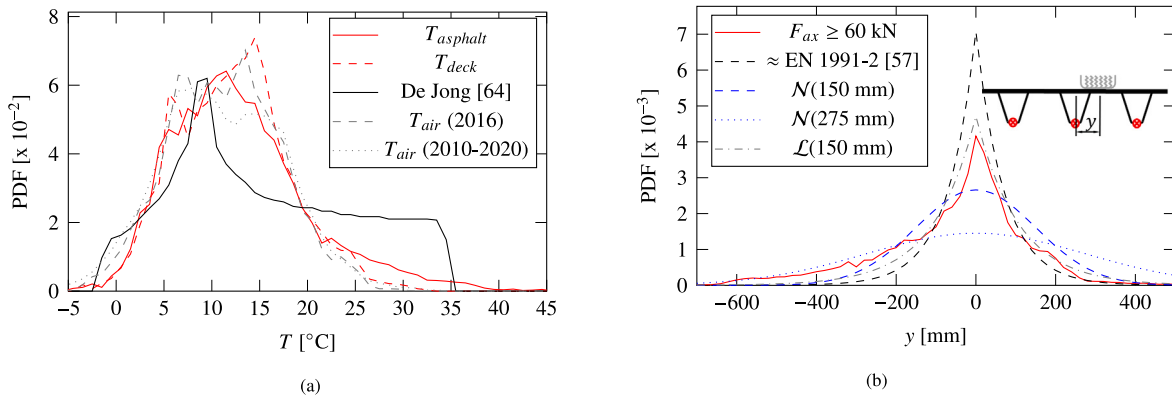
**Fig. 15.** PDF of vehicles with $F_{ax} \geq 60$ kN compared with distributions by others: (a) As a function of temperature, where De Jong [64] overestimates the fractions at high temperatures; (b) As a function of the transverse location, with large differences between studies.
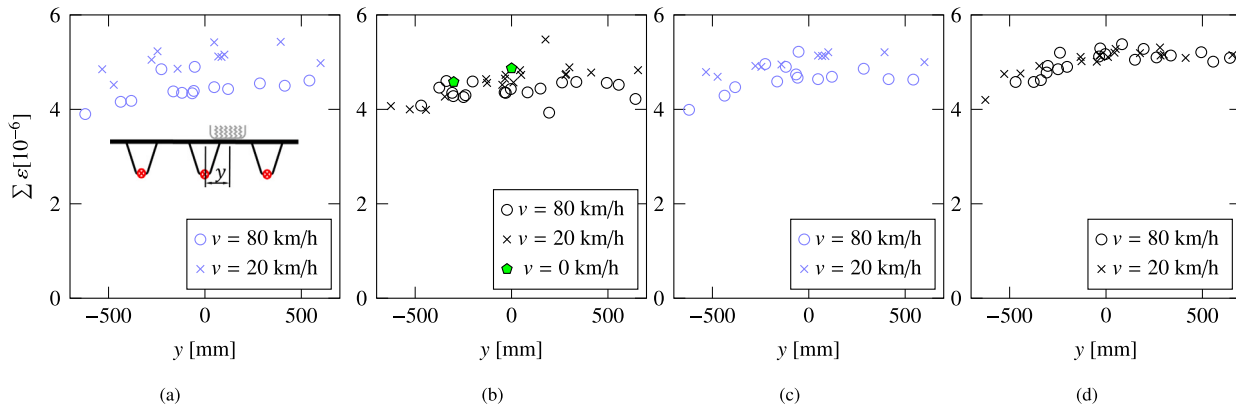


**Fig. 16.** Summed strains at the rib bottoms: (a) SG1–3 during summer night; (b) SG1–3 during winter night; (c) SG34/35/37 during summer night; (d) SG34/35/37 during winter night. Except for subfigure (d), the average summed strain is higher at 20 km/h than at 80 km/h, attributed to dynamic interaction between OBD and vehicle.

because ageing increases asphalt stiffness [68], whereas asphalt fatigue may reduce it [69]. Comparing the studies [13,15,23,25–31,70], the influence of temperature reduces (or is even negligible) for thicker deck plate and thinner asphalt layers and vice versa.

With respect to the transverse location, most studies assume a Gaussian distribution with a standard deviation either taken from standards or measured and ranging between 150 and 275 mm [36,41,71–73] (denoted as $\mathcal{N}(150$–$275$ mm)). Yan et al. [51] uses a different distribution, with a distinct peak and heavy tails. Blab [74] proposes a Laplace distribution with a standard deviation between 100 and 200 mm ($\mathcal{L}(100$–$200$ mm)). Fig. 15(b) gives the range of distributions, showing large differences between studies. Using the algorithm in Appendix, this study reveals that the distribution correlates with axle load. A subset with 45 kN $\leq F_{ax} \leq 60$ kN gives a multi-mode distribution with a larger standard deviation than the subset $F_{ax} > 60$ kN (210 mm versus 185 mm). The relatively narrow distribution of the latter subset is attributed to the uniformity in axle width for heavy vehicles and to asphalt rutting, causing heavy vehicles to automatically follow the track. The dependency on the vehicle load of the transverse location distribution has not been recognised by the studies mentioned above and it might be a cause of the large variation in standard deviations reported.

### 5.2. Dynamic vehicle–bridge interaction

The influence of vehicle speed on OBD strains appears non-negligible. Section 3.1 already showed the effect of the strain rate dependency of the asphalt Youngs modulus. Fig. 16 provides the summed maximum strains of the rear axle of the single vehicle tests of SG1–3

and SG34/35/37, respectively, as a function of the transverse location. In addition to scatter, the figure demonstrates a lower summed strain at high-speed compared to low-speed crossings, except for subfigure (d). This is not likely the result of asphalt stiffness, because the asphalt contributes only marginally to the elastic section modulus of the bottom of the ribs in longitudinal direction. Dynamic interaction between the vehicle and the OBD appears important. The deck vibrates due to vehicle crossing and with the vehicles used in the tests, it appears that the troughs of the vibrations coincide with the peaks of the static part of the response. This is observed both at low and at high speed, but the deck vibrations are larger at high speed, Fig. 17. The observation applies to all studied temperatures. As for the rear axle, the vibration troughs coincide with the peaks for the front axle but it is the opposite for the traction axle, which is an additional explanation for the underestimation of the strain of that axle with the model in Fig. 6. These findings are expected to be vehicle and speed specific.

Similar to the current study, strains in OBDs were measured during crossings of known vehicles at different speed in [21,22,37,61–63,70]. The strain differences between low and high-speed crossings ranged between negligible and $> 20\%$. The effects were either attributed to asphalt stiffness or to dynamic interaction, but not to both causes, which makes it difficult to separate their contributions. However, the collected data from literature and the current study make clear that the dynamic amplification is a random factor that is different per crossing axle.

The harmonic vibration of the deck at crossings with $v = 80$ km/h has an amplitude of maximum 0.15 times the peak strain for the location 4.5 m from the expansion joint (and approximately half the value for the location 28 m from the expansion joint). The corresponding Coefficient Of Variation (COV) of the amplification is $0.15/\sqrt{2} =$
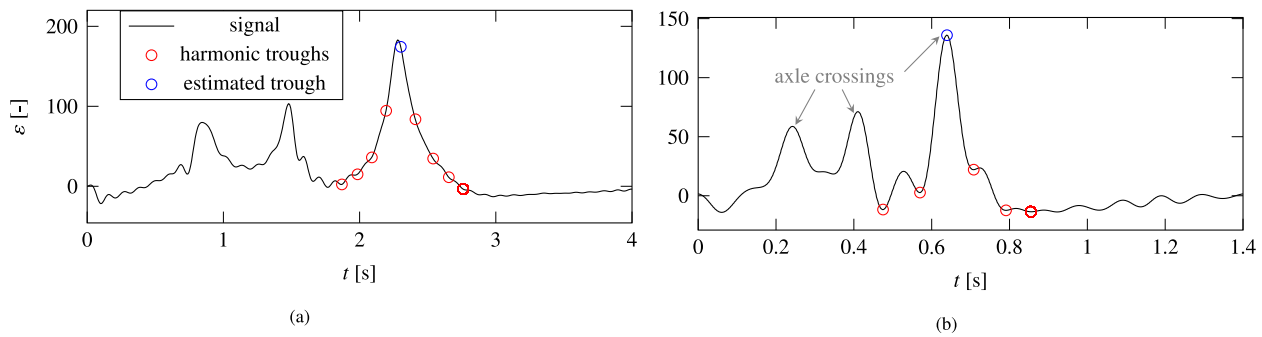
**Fig. 17.** Measured strains of two single vehicle tests with harmonic vibration highlighted: (a) at $v = 20$ km/h; (b) at $v = 80$ km/h. Red dots represent identified troughs of the harmonic vibration and blue dots are intermediate troughs estimated from periodicity. The estimated blue troughs coincide with the rear axle peaks of the static response.

0.10. This is used as an estimate of the dynamic factor. Its influence on the fatigue damage is estimated by multiplying each stress range predicted with the model and the WIM database with a random factor following a lognormal distribution with a mean of 1 and the COV of 0.10. The resulting fatigue damage is only 8% higher than the damage without the random factor. This is equivalent to a constant dynamic amplification factor applied to all stress ranges of 1.02. The factor is much smaller than the dynamic amplification factor of 1.2 implicitly incorporated in FLM4 of EN 1991-2 [57] and the additional factor of 1.08 at 4.5 m from the expansion joint. The factor of 1.75 and its reduction to 1.15 for details other than joints – provided justified by proof – as given in AASHTO [75] also appears conservative for fatigue design of OBDs. Finally, the amplification factors following from this and other measurement studies are smaller than estimates from computer simulation in [16,36].

### 5.3. Model uncertainty (MU)

The MU is estimated by dividing the measured strain of the single vehicle tests by the predicted strain using the FE model for the same scenario (temperature, load and transverse location). To separate the MU and the dynamic effects, the measured strains are first corrected by subtracting the estimated harmonic vibration (with an amplitude of 15% of the peak value). It then appears that the engineering model is able to predict the strains with reasonable accuracy: the MU is between 0.75 and 1 for most of the measurements with relatively high strain ranges. Additional data are available from other OBD studies, with the MU obtained from their data in a similar way as here:

- The MU based on 24 measurement locations was 0.98 on average with a SD of 0.04 in [76].
- The model underestimated the strain with approximately 10% in [26] for the lowest vehicle speed (giving the highest strain level), but the deviation was larger for higher speeds.
- In [36], the stress at the rib bottom was 2 MPa lower in the tests compared to the model, adding up to a MU of 0.87 because of the low stress level. The deck plate strains were significantly different in that study, attributed to the absence of asphalt in the FE model.
- Liu et al. [28] show a good agreement between measured and predicted strain, but it is unknown if the example given in their study is representative of all data.
- Zhu et al. [21] report a good agreement between test and model, but numbers are not given.

However, some of these studies used more detailed models than typically observed in engineering practice, or they used data that are generally not available to engineers (such as the stiffness properties of the specific asphalt mixture applied). In addition, it is unknown if models in these studies were adjusted after the measurement, based on its results. Further, the effect of dynamics – which is considered

separately here – is unknown for studies without crawling vehicle tests. This makes that the data should be treated with caution.

Despite these unknown factors or shortcomings, as a general trend, the MU data of the current study and that of the literature are close to the bounds of the MU distributions set in international guidelines. The JCSS probabilistic model code [47], as an example, recommends a MU with a mean of 1 and a standard deviation of 0.1 for global stress, further multiplied with a second MU with a mean of 1 and a standard deviation of 0.2 for hot-spot stress. The model deviations of OBDs are larger than those of other fatigue-sensitive (bridge) structures, see Section 1, attributed to the complicated load transfer in OBDs. However, as pointed out by the large differences in damage in Table 5, engineering assumptions for asphalt stiffness, temperature, transverse location, and load model are usually conservative, causing conservative damage estimates.

## 6. Conclusions

Strains predicted with an engineering FE model have been compared with measured strains in an OBD. The measurements were carried out with a single vehicle with known load at various temperatures and transverse location and with flowing traffic during one year of normal bridge operation.

The asphalt significantly influences the strains in the OBD for the two measured details. It causes the load to be shared between adjacent ribs (relevant to the rib bottom) and it influences the deck plate bending stiffness between the rib webs (relevant to the rib-to-deck weld). The asphalt stiffness depends on temperature and strain rate. For the deck of study (deck plate thickness of 12 mm, nominal asphalt thickness of 70 mm), the average theoretical fatigue damage caused by a vehicle is more than 15 times higher at $T_{asphalt} > 40°C$ compared to $T_{asphalt} < -5°C$ for the rib bottom location. This ratio is even $> 10^4$ for the deck plate location. The ratios will be lower for thicker deck plates and thinner asphalt surfaces.

The transverse location of the fatigue relevant, heavy vehicles can be approximated by a Laplace distribution with a standard deviation of 185 mm. This distribution is narrower than that of all vehicles, caused by asphalt rutting and the uniform transverse wheel distance of heavy vehicles. The distribution incorporated in the Eurocode fatigue load models appears too narrow and the distributions used in most other studies are too wide, the latter attributed to ignoring the influence of vehicle load.

Deck vibrations caused by vehicles amplify or reduce the static load effect. The effect can be considered as a random load factor with a mean close to 1. The constant dynamic amplification factor of 1.2 implicitly incorporated in the Eurocode fatigue load models is too conservative (however, conservatism is required for meeting sufficient reliability).

Strains in an OBD can be predicted with reasonable accuracy using an engineering FE model. The MU is close to the bounds set by international guidelines for a given load scenario and asphalt stiffness.
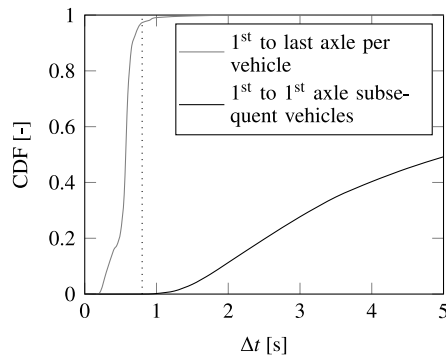
**Fig. A.18.** Time intervals between passing axles of the raw WIM database. A negligible number of vehicles have a time interval smaller than $\Delta t = 0.8$ s with their predecessor, whereas the interval between the first and last axle of a single vehicle is almost always smaller than $\Delta t = 0.8$ s.

However, the damage prediction highly depends on the engineering choices of asphalt stiffness, transverse location distribution, and load model. Engineering assumptions usually result in conservative damage estimates.

## CRediT authorship contribution statement

**Johan Maljaars:** Conceptualization, Methodology, Formal analysis (of flowing traffic measurements), Writing – original draft preparation. **Stefan Verdenius:** Formal analysis (of single vehicle tests), Writing – reviewing. **Henco Burggraaf:** Resources (Finite element modelling). **Sjors van Es:** Resources (Measurements), Writing – reviewing.

## Declaration of competing interest

The authors declare that they have no known competing financial interests or personal relationships that could have appeared to influence the work reported in this paper.

## Data availability

Data will be made available on request.

## Acknowledgements

## Appendix. Algorithm for the transverse location

To compensate for the influence of thermal expansion, the 10-minutes mode of the strain was subtracted from the strain signal prior to rainflow counting. Whereas this had a negligible influence on the strain spectra, it implied that axles of heavy vehicles were clearly distinguishable by peaks (or troughs) in the strain histories. To estimate the number of heavy vehicles $N_{obs}$, an algorithm is needed that determines if a peak (or trough) is related to the first axle of a new vehicle or caused by a subsequent axle of a single (already detected) vehicle. To this end, the time intervals between subsequent axles passing the WIM station were evaluated. Fig. A.18 gives the Cumulative Distribution Function (CDF) of the time intervals between the first axles of subsequent vehicles (black) and between the first and the last axle of each vehicle (grey). A criterion of $\Delta t = 0.8$ s between subsequent peaks (or troughs) was applied to distinguish the first axle per vehicle from other axles: more than 99% of the vehicles has a time interval with their predecessor exceeding 0.8 s, whereas less than 3% of the vehicles have a time interval between the first and last axle exceeding 0.8 s. Raw WIM data were used for the time intervals, implying that the data contain both normal speed and low speed (traffic jam) crossings.

Subsequently, a criterion is required to determine if a peak (or trough) in the signal belongs to a heavy vehicle. The first axle of the WIM-recorded heavy vehicles with a speed larger than 30 km/h – for which the WIM data are reliable – has a mean axle load of 58 kN with a standard deviation of 11 kN. The 90% exceedance fraction of the axle load of the first axle is 45 kN. This axle load – hence a tyre load of 22.5 kN – was used to distinguish heavy vehicles from other vehicles. Irrespective of temperature and for almost all transverse locations, the sum of the strains of SG1–3 per unit tyre load of the first axle as determined with the single vehicle tests (Section 3.1) is $4.6 \cdot 10^{-6}$/kN or slightly higher. A peak in the signal was therefore associated with the front tyre of a new vehicle if the time interval with the previous identified vehicle exceeds 0.8 s and if the sum of the strain of SG1–3 exceeds $105 \cdot 10^{-6}$.

The transverse location was estimated by the ratio of strain of SG1–3. The single vehicle tests during the winter night described in Section 3.1 were used to establish the relationship because the transverse location of the vehicle was recorded more accurately in these tests compared to the summer tests. Fig. A.19(a) gives the ratio of strain of each of the gauges SG1–3, $\varepsilon_i$, and the average strain of SG1–3, $\varepsilon_{av}$, as a function of the recorded transverse location of the winter night tests, revealing a clear correlation between the strain gauge ratios and the location. Based on this, the algorithm given in Fig. A.20 was developed for estimating the transverse location. Fig. A.19(b) provides the estimated location using the algorithm, $y_{pred}$, and the measured location, $y$, of all tests. A high coefficient of determination results: $R^2 = $
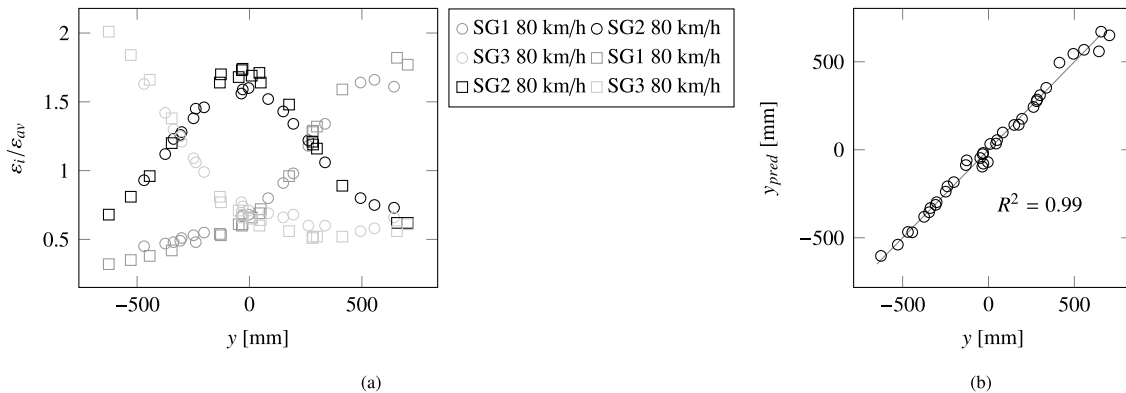


(a)



(b)

**Fig. A.19.** Estimate of the transverse location: (a) Relation between measured transverse location and relative strains of gauges SG1–3, used to establish the algorithm of Fig. A.20; (b) Measured transverse location versus transverse location predicted with the algorithm of Fig. A.20. A high coefficient of determination equal to $R^2 = 0.99$ results.
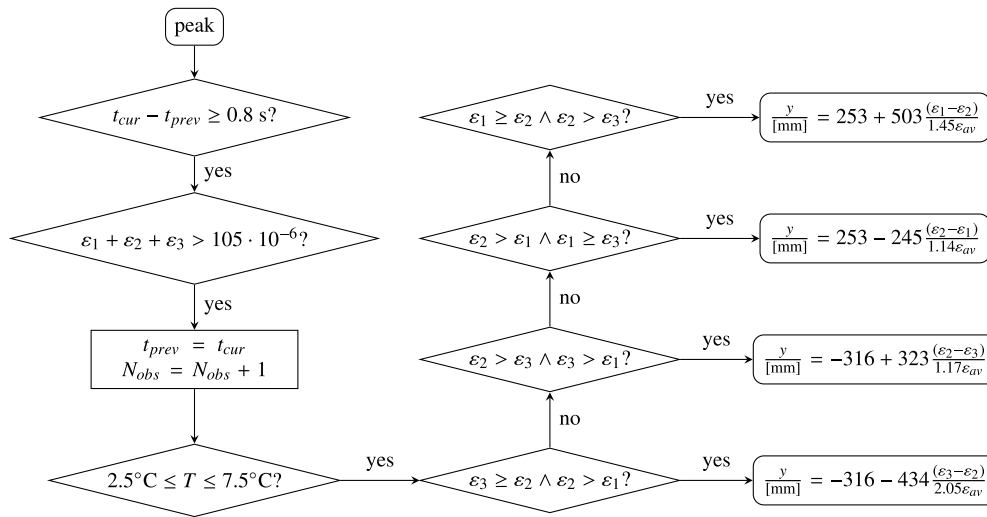
**Fig. A.20.** Flowchart to predict the transverse location, where $t_{cur}$ and $t_{prev}$ are the times of the current and previous peak, respectively.

0.99. The distribution of the transverse location of the flowing traffic was determined for vehicles crossing at a deck temperature between $2.5°C \leq T \leq 7.5°C$, similar to the winter night tests and amounting to 20% of $N_{obs}$.

## References

[1] R. Wolchuk, Lessons from weld cracks in orthotropic decks on three European bridges, J. Struct. Eng. 116 (1) (1990) 75–84.

[2] Q. Zhang, Y. Bu, Q. Li, Review on fatigue problems of orthotropic steel bridge deck, China J. Highway Transp. 30 (3) (2017) 14–30.

[3] M. Kolstein, J. Cuninghame, A. Bruls, S. Caramelli, H. Lehrke, B. Jacob, European research on the improvement of the fatigue resistance and design of steel orthotropic bridge decks, in: Advances in Steel Structures, ICASS'96, 1996, pp. 541–546.

[4] K. Yokozeki, C. Miki, Fatigue evaluation for longitudinal-to-transverse rib connection of orthotropic steel deck by using structural hot spot stress, Weld World 60 (2016) 83–92.

[5] N. Iqbal, H. Fang, A. Naseem, M. Kashif, H. De Backer, A numerical evaluation of structural hot-spot stress methods in rib-to-deck joint of orthotropic steel deck, Appl. Sci. 10 (19) (2020) 6924.

[6] P. Wang, X. Pei, P. Dong, S. Song, Traction structural stress analysis of fatigue behaviors of rib-to-deck joints in orthotropic bridge deck, Int. J. Fatigue 125 (2019) 11–22.

[7] H. Yang, P. Wang, H. Qian, P. Dong, Analysis of fatigue test conditions for reproducing weld toe cracking into U-rib wall in orthotropic bridge decks, Int. J. Fatigue 162 (2022) 106976.

[8] Q.-H. Zhang, C. Cui, Y.-Z. Bu, Y.-M. Liu, H.-W. Ye, Fatigue tests and fatigue assessment approaches for rib-to-diaphragm in steel orthotropic decks, J. Constr. Steel Res. 114 (2015) 110–118.

[9] J. Heng, K. Zheng, C. Gou, Y. Zhang, Y. Bao, Fatigue performance of rib-to-deck joints in orthotropic steel decks with thickened edge U-ribs, J. Bridge Eng. 22 (9) (2017) 04017059.

[10] T.S. 1993-1-901, Fatigue Design of Orthotropic Bridge Decks with the Hot Spot Stress Method (Final Draft), CEN, 2023.

[11] J. Maljaars, R. Pijpers, W. Wu, H. Kolstein, Fatigue resistance of rib to deck, crossbeam to deck and deck to deck welds in orthotropic decks using structural stress, Int. J. Fatigue (2023) 107742.

[12] Z. Zhu, Z. Xiang, J. Li, A. Carpinteri, Fatigue damage investigation on diaphragm cutout detail on orthotropic bridge deck based on field measurement and FEM, Thin-Walled Struct. 157 (2020) 107106.

[13] J. Di, X. Ruan, X. Zhou, J. Wang, X. Peng, Fatigue assessment of orthotropic steel bridge decks based on strain monitoring data, Eng. Struct. 228 (2021) 111437.

[14] C. Cheng, X. Xie, W. Yu, Investigation of the fatigue stress of orthotropic steel decks based on an arch bridge with the application of the Arlequin method, Materials 14 (24) (2021) 7653.

[15] F. Machida, T. Yuge, C. Miki, E. Yamaguchi, T. Shimozato, Stress measurements on fatigue-damaged structures with orthotropic steel decks in summer and winter, in: Proc 1st Int Orthotropic Bridge Deck, ASCE, 2004, pp. 569–584.

[16] R.C. Battista, M.S. Pfeil, E.M. Carvalho, Vehicle-structure interaction effect on the fatigue life of steel orthotropic decks, in: Proc 8th Int Conf Struct Dynamics EURODYN, 2011, pp. 1489–1496.

[17] H.-B. Sim, C.-M. Uang, Stress analyses and parametric study on full-scale fatigue tests of rib-to-deck welded joints in steel orthotropic decks, J. Bridge Eng. 17 (5) (2012) 765–773.

[18] R. Liu, B. Ji, M. Wang, C. Chen, H. Maeno, Numerical evaluation of toe-deck fatigue in orthotropic steel bridge deck, J. Perform. Constr. Fac. 29 (6) (2015) 04014180.

[19] M. Li, Y. Suzuki, K. Hashimoto, K. Sugiura, Experimental study on fatigue resistance of rib-to-deck joint in orthotropic steel bridge deck, J. Bridge Eng. 23 (2) (2018) 04017128.

[20] L. Zhang, H. Zhao, E.J. OBrien, X. Shao, Virtual monitoring of orthotropic steel deck using bridge weigh-in-motion algorithm: Case study, Struct. Health Monit. 18 (2) (2019) 610–620.

[21] Z. Zhu, J. Li, X. Chen, A. Carpinteri, Stress behaviors of rib-to-deck double-sided weld detail on orthotropic steel deck, J. Constr. Steel Res. 187 (2021) 106947.

[22] J. Li, Z. Zhu, Stress behaviors at rib-to-floorbeam weld and cutout details under controlled truck loading, Appl. Sci. 12 (6) (2022) 3012.

[23] B. Ji, R. Liu, C. Chen, H. Maeno, X. Chen, Evaluation on root-deck fatigue of orthotropic steel bridge deck, J. Constr. Steel Res. 90 (2013) 174–183.

[24] J.D. Rodenburg, J. Maljaars, S.T. Hengeveld, A.H. Vervuurt, Tyre contact surface for the fatigue design of orthotropic steel bridge decks, Eng. Struct. 283 (2023) 115869.

[25] Z.-G. Xiao, K. Yamada, S. Ya, X.-L. Zhao, Stress analyses and fatigue evaluation of rib-to-deck joints in steel orthotropic decks, Int. J. Fatigue 30 (8) (2008) 1387–1397.

[26] S. Pouget, C. Sauzéat, H. Di Benedetto, F. Olard, Modeling of viscous bituminous wearing course materials on orthotropic steel deck, Mater. Struct. 45 (2012) 1115–1125.

[27] Y. Song, Y. Ding, Fatigue monitoring and analysis of orthotropic steel deck considering traffic volume and ambient temperature, Sci. China Technol. Sci. 56 (2013) 1758–1766.

[28] Y. Liu, H. Zhang, Y. Liu, Y. Deng, N. Jiang, N. Lu, Fatigue reliability assessment for orthotropic steel deck details under traffic flow and temperature loading, Eng. Fail. Anal. 71 (2017) 179–194.

[29] I. Farreras-Alcover, M.K. Chryssanthopoulos, J.E. Andersen, Data-based models for fatigue reliability of orthotropic steel bridge decks based on temperature, traffic and strain monitoring, Int. J. Fatigue 95 (2017) 104–119.

[30] H. Cheng, L. Liu, L. Sun, Determination of layer modulus master curve for steel deck pavement using field-measured strain data, Transp. Res. Rec. 2673 (2) (2019) 617–627.

[31] H. Cheng, L. Liu, L. Sun, Critical response analysis of steel deck pavement based on viscoelastic finite element model, Int. J. Pavement. Eng. 22 (3) (2021) 307–318.

[32] F. De Jong, M. Kolstein, Strengthening a bridge deck with high performance concrete, in: Proc Orthotropic Bridge Conference, 2004, pp. 328–347.

[33] R. Walter, J.F. Olesen, H. Stang, T. Vejrum, Analysis of an orthotropic deck stiffened with a cement-based overlay, J. Bridge Eng. 12 (3) (2007) 350–363.

[34] X. Shao, D. Yi, Z. Huang, H. Zhao, B. Chen, M. Liu, Basic performance of the composite deck system composed of orthotropic steel deck and ultrathin RPC layer, J. Bridge Eng. 18 (5) (2013) 417–428.

[35] S. Qin, J. Zhang, C. Huang, L. Gao, Y. Bao, Fatigue performance evaluation of steel-UHPC composite orthotropic deck in a long-span cable-stayed bridge under in-service traffic, Eng. Struct. 254 (2022) 113875.

[36] R.C. Battista, M.S. Pfeil, E.M. Carvalho, Fatigue life estimates for a slender orthotropic steel deck, J. Constr. Steel Res. 64 (1) (2008) 134–143.

[37] Z.-G. Xiao, K. Yamada, J. Inoue, K. Yamaguchi, Measurement of truck axle weights by instrumenting longitudinal ribs of orthotropic bridge, J. Bridge Eng. 11 (5) (2006) 526–532.

[38] R. Ma, Z. Zhang, Y. Dong, Y. Pan, Deep learning based vehicle detection and classification methodology using strain sensors under bridge deck, Sensors 20 (18) (2020) 5051.

[39] C.-Y. Li, C. Wang, Q.-X. Yang, T.-Y. Qi, Identification of vehicle loads on an orthotropic deck steel box beam bridge based on optimal combined strain influence lines, Appl. Sci. 12 (19) (2022) 9848.

[40] Y. Deng, A. Li, D. Feng, Fatigue reliability assessment for orthotropic steel decks based on long-term strain monitoring, Sensors 18 (1) (2018) 181.

[41] C. Cui, Q. Zhang, Y. Luo, H. Hao, J. Li, Fatigue reliability evaluation of deck-to-rib welded joints in OSD considering stochastic traffic load and welding residual stress, Int. J. Fatigue 111 (2018) 151–160.

[42] J. Maljaars, D. Leonetti, B. Hashemi, H. Snijder, Systematic derivation of safety factors for the fatigue design of steel bridges, Struct. Saf. 97 (2022) 102229.

[43] A. Nussbaumer, V. Grigoriou, Round robin on local stress evaluation for fatigue by various fem software, in: 69th International Institute for Welding (IIW) Annual Assembly and International Conference, 2016, IIW doc XIII–2650–16.

[44] W. Fricke, Recommended hot-spot analysis procedure for structural details of ships and FPSOs based on round-robin FE analyses, Int. J. Offshore Polar. 12 (01) (2002).

[45] W. Fricke, A. Kahl, Comparison of different structural stress approaches for fatigue assessment of welded ship structures, Mar. Struct. 18 (7–8) (2005) 473–488.

[46] W. Fricke, Round-robin study on stress analysis for the effective notch stress approach, Weld World 51 (3) (2007) 68–79.

[47] JCSS, Probabilistic Model Code, Tech. Rep., Joint Committee of Structural Safety, 2013, URL https://www.jcss-lc.org/jcss-probabilistic-model-code.

[48] DNV, DNV-RP-C210 Probabilistic Methods for Planning of Inspection for Fatigue Cracks in Offshore Structures, Tech. Rep., Det Norske Veritas, 2019.

[49] O. Ditlevsen, H.O. Madsen, Structural Reliability Methods, Tech. Rep., Technical University of Denmark, 2007.

[50] DIANA 9.4.4 user manual, 2023, URL https://dianafea.com/diana-manuals/.

[51] F. Yan, W. Chen, Z. Lin, Prediction of fatigue life of welded details in cable-stayed orthotropic steel deck bridges, Eng. Struct. 127 (2016) 344–358.

[52] S. Wei, Z. Zhang, S. Li, H. Li, Strain features and condition assessment of orthotropic steel deck cable-supported bridges subjected to vehicle loads by using dense FBG strain sensors, Smart Mater. Struct. 26 (10) (2017) 104007.

[53] T.W. Kim, J. Baek, H.J. Lee, S.Y. Lee, Effect of pavement design parameters on the behaviour of orthotropic steel bridge deck pavements under traffic loading, Int. J. Pavement. Eng. 15 (5) (2014) 471–482.

[54] H. Verburg, F. Van Gogh, Determining Dynamic Stiffness Modli and Phase Angles of Porous Asphalt and Mastic Asphalt (In Dutch); Report IR-R-96.042, Tech. Rep., Dienst Weg- en Waterbouw, 1996.

[55] E. Kassem, Z.C. Grasley, E. Masad, Viscoelastic Poisson's ratio of asphalt mixtures, Int. J. Geomech. 13 (2) (2013) 162–169.

[56] Q.T. Nguyen, H. Di Benedetto, Q.P. Nguyen, T.T.N. Hoang, et al., Effect of time–temperature, strain level and cyclic loading on the complex Poisson's ratio of asphalt mixtures, Constr. Build. Mater. 294 (2021) 123564.

[57] E.N. 1991-2, Eurocode 1: Actions on Structures - Part 2: Traffic Loads on Bridges, CEN, 2003.

[58] J. Maljaars, Evaluation of traffic load models for fatigue verification of European road bridges, Eng. Struct. 225 (2020) 111326.

[59] A. Palmgren, Die Lebensdauer von kugellagern, VDI Z 68 (1924) 339–341.

[60] M.A. Miner, Cumulative damage in fatigue, Trans. ASME (1945) A159–A164.

[61] X.G. Liu, X.X. Zhao, Y.L. Zhang, Research on static and dynamic tests of steel orthotropic decks, Appl. Mech. Mater. 94 (2011) 1291–1297.

[62] S. Pouget, C. Sauzéat, H. Di Benedetto, F. Olard, Millau viaduct response under static and moving loads considering viscous bituminous wearing course materials, in: 7th RILEM International Conference on Cracking in Pavements: Mechanisms, Modeling, Testing, Detection and Prevention Case Histories, 2012, pp. 223–232.

[63] L. Zhang, H. Zhao, X. Shao, Vehicle-bridge interaction analysis of orthotropic steel deck bridge in fatigue details, J. Hunan Univ. 43 (11) (2016) 26–32 (in Chinese).

[64] F. De Jong, Renovarion Techniques for Fatigue Cracked Orthotropic Steel Bridge Decks (Ph.D. thesis), Delft University of Technology, 2006.

[65] T.O. Medani, Design Principles of Surfacings on Orthotropic Steel Bridge Decks (Ph.D. thesis), Delft University of Technology, 2006.

[66] J. Maljaars, F. van Dooren, M. Kolstein, Fatigue assessment for deck plates in orthotropic bridge decks, Steel. Constr. 5 (2) (2012) 93–100.

[67] KNMI, 2023, URL https://www.knmi.nl/nederland-nu/klimatologie/uurgegevens/. (Accessed: 06 November 2023).

[68] P.K. Das, H. Baaj, S. Tighe, N. Kringos, Atomic force microscopy to investigate asphalt binders: A state-of-the-art review, Road Mater. Pavement. 17 (3) (2016) 693–718.

[69] R. Lundstrom, H. Di Benedetto, U. Isacsson, Influence of asphalt mixture stiffness on fatigue failure, J. Mater. Civil Eng. 16 (6) (2004) 516–525.

[70] R.J. Connor, J.W. Fisher, In-service response of an orthotropic steel deck compared with design assumptions, Transp. Res. Rec. 1696 (1) (2000) 100–108.

[71] A. Vrouwenvelder, O. Dijkstra, R. Van Foeken, 99-CON-DYN-R0108 Basic Philosophy for the Design of Road Bridges, Part: Fatigue of Steel Bridge Decks, Probabilistic Design Philosophy, Tech. Rep., TNO, 2000 (in Dutch).

[72] B.H. Oh, Y. Lew, Y.C. Choi, Realistic assessment for safety and service life of reinforced concrete decks in girder bridges, J. Bridge Eng. 12 (4) (2007) 410–418.

[73] C. Cui, Y. Bu, Y. Bao, Q. Zhang, Z. Ye, Strain energy-based fatigue life evaluation of deck-to-rib welded joints in OSD considering combined effects of stochastic traffic load and welded residual stress, J. Bridge Eng. 23 (2) (2018) 04017127.

[74] R. Blab, The Transverse Distribution as an Influencing Factor in the Dimensioning of the Road, Tech. Rep., Vienna Technical University, 1995 (in German).

[75] AASHTO, LRFD Bridge Design Specifications, American association of state highway and transportation officials, 2012.

[76] L. Zhang, Orthotropic Steel Deck Bridge Dynamic Response and Loads Identification of Vehicles (Ph.D. thesis), Hunan University, 2017 (in Chinese).